



Construction of emissive ruthenium(II) metallacycle over 1000 nm wavelength for in vivo biomedical applications

Yuling Xu^{1,6}, Chonglu Li^{1,6}, Shuai Lu^{2,3}, Zhizheng Wang^{1,4}, Shuang Liu⁵, Xiujun Yu^{2,3}, Xiaopeng Li^{2,3} [✉] & Yao Sun¹ [✉]

Although Ru(II)-based agents are expected to be promising candidates for substituting Pt-drug, their in vivo biomedical applications are still limited by the short excitation/emission wavelengths and unsatisfactory therapeutic efficiency. Herein, we rationally design a Ru(II) metallacycle with excitation at 808 nm and emission over 1000 nm, namely **Ru1085**, which holds deep optical penetration (up to 6 mm) and enhanced chemo-phototherapy activity. In vitro studies indicate that **Ru1085** exhibits prominent cell uptake and desirable anticancer capability against various cancer cell lines, especially for cisplatin-resistant A549 cells. Further studies reveal **Ru1085** induces mitochondria-mediated apoptosis along with S and G2/M phase cell cycle arrest. Finally, **Ru1085** shows precise NIR-II fluorescence imaging guided and long-term monitored chemo-phototherapy against A549 tumor with minimal side effects. We envision that the design of long-wavelength emissive metallacycle will offer emerging opportunities of metal-based agents for in vivo biomedical applications.

¹Key Laboratory of Pesticides and Chemical Biology, Ministry of Education, International Joint Research Center for Intelligent Biosensor Technology and Health, College of Chemistry, Central China Normal University, Wuhan, Hubei 430079, China. ²Shenzhen University General Hospital, Shenzhen University Clinical Medical Academy, Shenzhen, Guangdong 518055, China. ³College of Chemistry and Environmental Engineering, Shenzhen University, Shenzhen, Guangdong 518060, China. ⁴Guangdong Provincial Key Laboratory of Luminescence from Molecular Aggregates, South China University of Technology, Guangzhou, Guangdong 510640, China. ⁵School of Materials Science and Engineering, Wuhan University of Technology, Wuhan, Hubei 430070, China. ⁶These authors contributed equally: Yuling Xu, Chonglu Li. ✉email: xiaopengli@szu.edu.cn; sunyaogbasp@mail.ccnu.edu.cn

Ruthenium (Ru) complexes were identified as ideal chemotherapy agents for cancer treatment due to their lower nonspecific toxicities and higher activities against Pt-drug-resistant cancer cells^{1–4}. More recently, the utilization of Ru(II)-polypyridyl complexes as photodynamic therapy (PDT) agents has further ameliorated therapeutic efficiency to benefit anticancer practice^{5–9}. Despite the achieved success, some major issues of the current Ru(II) complexes still limited their widespread in vivo applications^{10,11}. First, the short excitation/emission wavelengths ($\lambda_{\text{ex}} < 600$ nm, $\lambda_{\text{em}} < 700$ nm) of reported Ru(II) complexes failed to efficiently penetrate deep tissues, which not only reduces the efficiency of phototherapy but also undermines in vivo precisely delineating lesion margin and real-time monitoring/evaluation of therapeutic effects^{12,13}. Second, single chemo- or phototherapy modality of Ru(II) complexes cannot simultaneously balance efficiency and safety^{14,15}. Besides, recent studies have revealed that macromolecular drugs (i.e., metallomacrocycles) possess superior cellular uptake and longer retention time in cancer cells compared to their small counterparts^{16–18}. As such, developing long-wavelength emissive Ru(II) macromolecules with combinational chemo-phototherapy is highly demanded to enable accurate in vivo cancer diagnosis and therapy.

Recently, a wide range of metallomacrocycles with variable shapes, sizes, and functionalities have been constructed by leveraging the coordination-driven self-assembly approach and drawn increasing attention in biomedicine^{19–23}. Among them, Ru(II) metallacycles have been successfully applied for the chemotherapeutic or phototherapeutic treatment of cancer^{24–28}. Noteworthy, Ru(II) metallacycles can selectively enter cancer cells with a long-term stay compared to normal cells^{29,30}. More importantly, the emission/excitation wavelength and phototherapy efficiency of metallacycles could be finely regulated by embedding well-designed fluorescent ligands without tedious chemical synthesis^{31–34}. However, it still remains challenging for in vivo noninvasively monitoring Ru(II) metallacycles delivery/biodistribution and therapeutic feedback in a timely manner owing to their emission/excitation wavelengths located in the visible light region (400–700 nm). Fortunately, recent development in fluorescent imaging was able to shift the wavelength into the second near-infrared region (NIR-II, 1000–1700 nm), which holds deeper tissue penetration and higher temporal-spatial resolution than traditional visible and NIR-I (700–900 nm) regions by minimizing auto-fluorescence and tissue scattering^{35–43}. Therefore, it is expected that the integration of NIR-II fluorescent ligands into the Ru(II) metallacycle could advance the corresponding applications in biomedicine.

Herein, we report a NIR-II emissive Ru(II) metallacycle (**Ru1085**, $\lambda_{\text{em}} = 1085$ nm) formed via coordination-driven self-assembly using NIR-II fluorescent ligand **1** and dinuclear areneruthenium **2** as the building blocks (Fig. 1). Due to the clear-cut advantages of NIR excitation and NIR-II emission, **Ru1085** exhibits deep tissue penetration (>6 mm) and imaging capability with high temporal-spatial resolution. **Ru1085** also possesses ultrahigh photothermal conversion efficiency (PCE = 30.9%) along with reactive oxygen species (ROS) generation capability, demonstrating prospects for efficient phototherapy. Notably, **Ru1085** shows desirable cellular uptake and high cytotoxicity to cisplatin-resistant A549 cells with low toxicity towards mammalian cells. Further in vivo studies successfully utilize **Ru1085** in NIR-II fluorescence imaging to precisely guide and monitor the effective chemo-phototherapy on A549 tumor-bearing mice with single-dose and single laser illumination for one treatment. Collectively, this study assembles a novel Ru(II) metallacycle with long excitation/emission wavelength for NIR-II fluorescence imaging-guided and monitored improved chemo-phototherapy towards tumors.

Results

Design, synthesis and characterization of Ru1085. Through molecular modeling and theoretical calculation, we introduced strong electron donor units (julolidinyl and anisole groups) and Ru(II) coordination units (thiophen-pyridine) into the acceptor aza-BODIPY skeleton to prepare NIR-II emissive ligand **1**. Because of the strong intramolecular charge transfer (ICT) from donor to acceptor, the emission wavelength of ligand **1** located on the NIR-II region (Supplementary Fig. 1), which was further confirmed by theoretical calculation (Supplementary Fig. 2). The ligand **1** was confirmed by nuclear magnetic resonance (NMR) and electrospray ionization mass spectrometry (ESI-MS) (Supplementary Figs. 3–5).

Metallacycle **Ru1085** was prepared by assembling NIR-II emissive ligand **1** and 0° Ru(II) acceptor **2**⁴⁴ in MeOH/CHCl₃ at room temperature for 24 h (Fig. 2a). The formation of **Ru1085** was then confirmed by ¹H/¹⁹F NMR, 2D rotating frame Overhauser effect spectroscopy (ROESY) and electrospray ionization time-of-flight mass spectrometry (ESI-TOF-MS). As seen in Fig. 2b, the protons of the pyridine from **Ru1085** showed diagnostic upfield shift compared with those of free ligand **1** due to the formation of the Ru–N bond. The protons of the *p*-cymene parts of **Ru1085** also shifted upfield compared with those of free Ru(II) acceptor **2** (Fig. 2b and Supplementary Figs. 6, 7), suggesting the coordination of nitrogen atoms to Ru(II) centers. The result of ¹⁹F NMR spectrum exhibited a single and sharp peak at –79.29 ppm, indicating the presence of free trifluoromesulfate counteranions in the same chemical environment (Supplementary Fig. 8). Besides, ROESY spectrum showed a strong cross peak between the pyridyl proton H_{1a} of ligand **1** and the proton H_{2c} from the *p*-cymene moiety of **Ru1085** (Supplementary Fig. 9). Then, ESI-TOF-MS further confirmed the formation of rectangular metallacycle **Ru1085** and exhibited two main peaks which were assigned to [2 + 2] assembly due to the loss of OTf[–] counterions ($m/z = 862.46$ for [**Ru1085**–4OTf]⁴⁺ and $m/z = 1199.27$ for [**Ru1085**–3OTf]³⁺ respectively; Fig. 2c and Supplementary Fig. 10). All the peaks matched well with their theoretical distributions. Finally, the geometry optimization of **Ru1085** was carried out in Gaussian 09 (Fig. 2d). The optimized geometry showed that the distance between the two Ru centers of Ru(II) acceptor **2** was 8.16 Å, which was shorter than that between the centroids of ligand **1** (21.66 Å). All above results supported the successful construction of **Ru1085**.

Photophysical, photodynamic and photothermal properties, and stability studies. Primarily, the absorption and emission spectra of **Ru1085** were measured in different solvents (Supplementary Fig. 11). As shown in Fig. 3a and Supplementary Table 1, **Ru1085** exhibited a broad absorption band and centered at around 874 nm (molar extinction coefficient, $\epsilon = 4.67 \times 10^4 \text{ M}^{-1} \text{ cm}^{-1}$); meanwhile, the maximum emission wavelength was ~1085 nm ($\lambda_{\text{ex}} = 808$ nm) in dichloromethane (DCM). Simultaneously, the relative fluorescence quantum yield (Φ_f) of **Ru1085** was calculated to be 0.084% (using IR-26 as reference). The NIR-II fluorescence signals of **Ru1085** was strongest under a 1000 nm long-pass (LP) filter (Fig. 3b). Hence, the 1000 nm LP filter was employed in further imaging studies. To verify the optical penetration merits, the optical penetration performance of **Ru1085** was evaluated in mimic tissue (1% intralipid) with a classic photosensitizer tris(2,2'-bipyridyl)ruthenium (II) [Ru(bpy)₃Cl₂] as contrast. NIR-II fluorescence signal of **Ru1085** was observed as the penetration depth increasing up to 6 mm. On the contrary, the fluorescence signal of Ru(bpy)₃Cl₂ almost became negligible with the penetration depth around 1 mm (Fig. 3c), attributed to the short absorption/emission wavelength (Fig. 3c and Supplementary Fig. 12). These results implied that

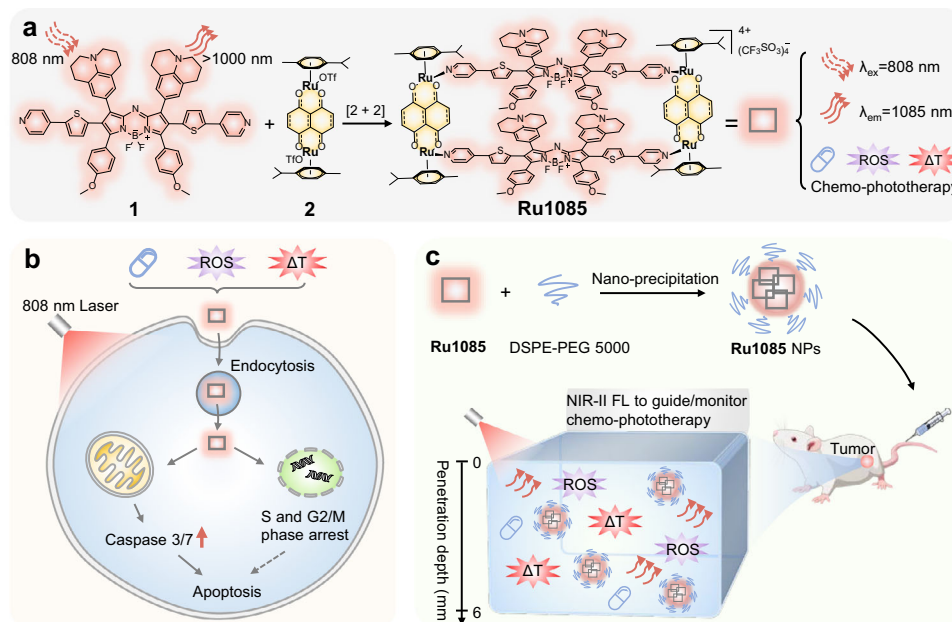


Fig. 1 Schematic illustration of the design, antitumor mechanism, and in vivo application of Ru1085. **a** The design, chemical structure, and properties of Ru1085, which is excited at 808 nm and emitted over 1000 nm with chemotherapeutic, photodynamic/photothermal properties. **b** The underlying antitumor mechanism illustrates the internalization of Ru1085 into A549 cells through endocytic pathway, and subsequently induces mitochondria-mediated apoptosis and arrested cell cycle at S and G2/M phase. **c** Ru1085 is utilized in NIR-II fluorescence imaging for guiding and monitoring chemo-phototherapy in tumor-bearing mice models.

metallacycle **Ru1085** with excitation at 808 nm and emission within the NIR-II biowindow could have a potential prospect for deep tissue in vivo imaging.

Encouraged by the photophysical property of **Ru1085**, we further investigated singlet oxygen (1O_2)/ROS production and photothermal conversion. Electron spin resonance (ESR) spectroscopy was employed to directly detect 1O_2 using 2,2,6,6-tetramethylpiperidine (TEMP) as the 1O_2 trapping agent. The time-dependent ESR spectra of **Ru1085** were characterized with a 1:1:1 triplet signal (Fig. 3d). The 1O_2 generation capability of **Ru1085** was further confirmed using 1,3-diphenyliso-benzofuran (DPBF) as indicator and the 1O_2 quantum yield (Φ_Δ) was measured to be 0.14 using indocyanine green (ICG) as reference (Supplementary Fig. 13)⁴⁵. ROS generation of **Ru1085** was detected with time-dependence (0–60 s) using a ROS probe 2,7-dichlorodihydrofluorescein diacetate (H_2 -DCFH) (Fig. 3e). Besides, the photothermal behavior of **Ru1085** was concentration-dependent (0–10 μ M) (Supplementary Fig. 14) with high PCE (30.9%)⁴⁶ (Fig. 3f), which was superior to existing photothermal agent such as ICG (15.8%)⁴⁷. Consequently, **Ru1085** could be an excellent photodynamic and photothermal agent.

Efficient photosensitizers should possess high stability. Metallacycle **Ru1085** exhibited good stability in both phosphate buffer saline (PBS) and 10% fetal bovine serum (FBS) within prolonged incubation time (7 days) (Fig. 3g and Supplementary Fig. 15). **Ru1085** showed no photodegradation under 808 nm laser illumination (0.4 W cm^{-2} , 30 min) in PBS (Supplementary Fig. 16). Furthermore, **Ru1085** exhibited excellent photothermal-stability with no significant decay of temperature in heating-cooling cycles (Fig. 3h).

Evaluation of cell uptake and localization. Prior to the cell experiments, the lipophilicity of **Ru1085** was determined by the octanol/water partition coefficient ($\log P_{o/w}$) to estimate the cell uptake efficiency. **Ru1085** was more lipophilic ($\log P_{o/w} = 1.18$)

than ligand **1** ($\log P_{o/w} = 0.54$) and Ru(II) acceptor **2** ($\log P_{o/w} = -0.79$), implying the cell uptake of **Ru1085** might be more effective⁴⁸. Cell imaging tests indicated that NIR-II fluorescence signal persistently enhanced over incubation time (3–24 h) after A549 cells incubated with **Ru1085** (Fig. 4a and Supplementary Fig. 17). Note that, NIR-II fluorescence signal of cells incubated with **Ru1085** was much stronger than that incubated with ligand **1**. The images illustrated that metallacycle **Ru1085** possessed satisfactory cell uptake and retention efficiency. Further colocalization images revealed that **Ru1085** primarily localized in lysosomes with a high Pearson correlation coefficient (PCC) of 0.71 (Fig. 4b), along with partial accumulation in mitochondria and nucleus (Supplementary Fig. 18). Apart from that, laser ablation inductively coupled plasma mass spectrometry (LA-ICP-MS) was employed for clarifying the cell uptake of Ru element within single-cell-level⁴⁹. Strong signal of ^{102}Ru was detected in A549 cells after incubated with **Ru1085** (Fig. 4c). Meanwhile, quantitative analysis was carried out by inductively coupled plasma mass spectrometry (ICP-MS). Consistent with the results of NIR-II fluorescence imaging, Ru accumulated in cells over time (3–24 h) and the majority of Ru was observed in lysosomes (Fig. 4d, e).

To identify the cellular uptake mechanism of **Ru1085**, cellular NIR-II fluorescence imaging was taken under different inhibition conditions. The internalization of **Ru1085** was significantly inhibited at 4 °C, as well as with co-incubation of the metabolic inhibitors (2-deoxy-D-glucose and oligomycin) and endocytosis inhibitor (NH_4Cl)⁵⁰, revealing that the cellular uptake was energy-dependent endocytosis (Supplementary Fig. 19). Furthermore, the endocytosis inhibitors including sucrose and methyl- β -cyclodextrin (M - β CD)⁵¹, which impair clathrin and caveolae-mediated endocytosis separately, were utilized to investigate the mechanism (Supplementary Fig. 19). The results indicated that **Ru1085** was mainly internalized into cells through a clathrin- and caveolae-mediated endocytic pathway.

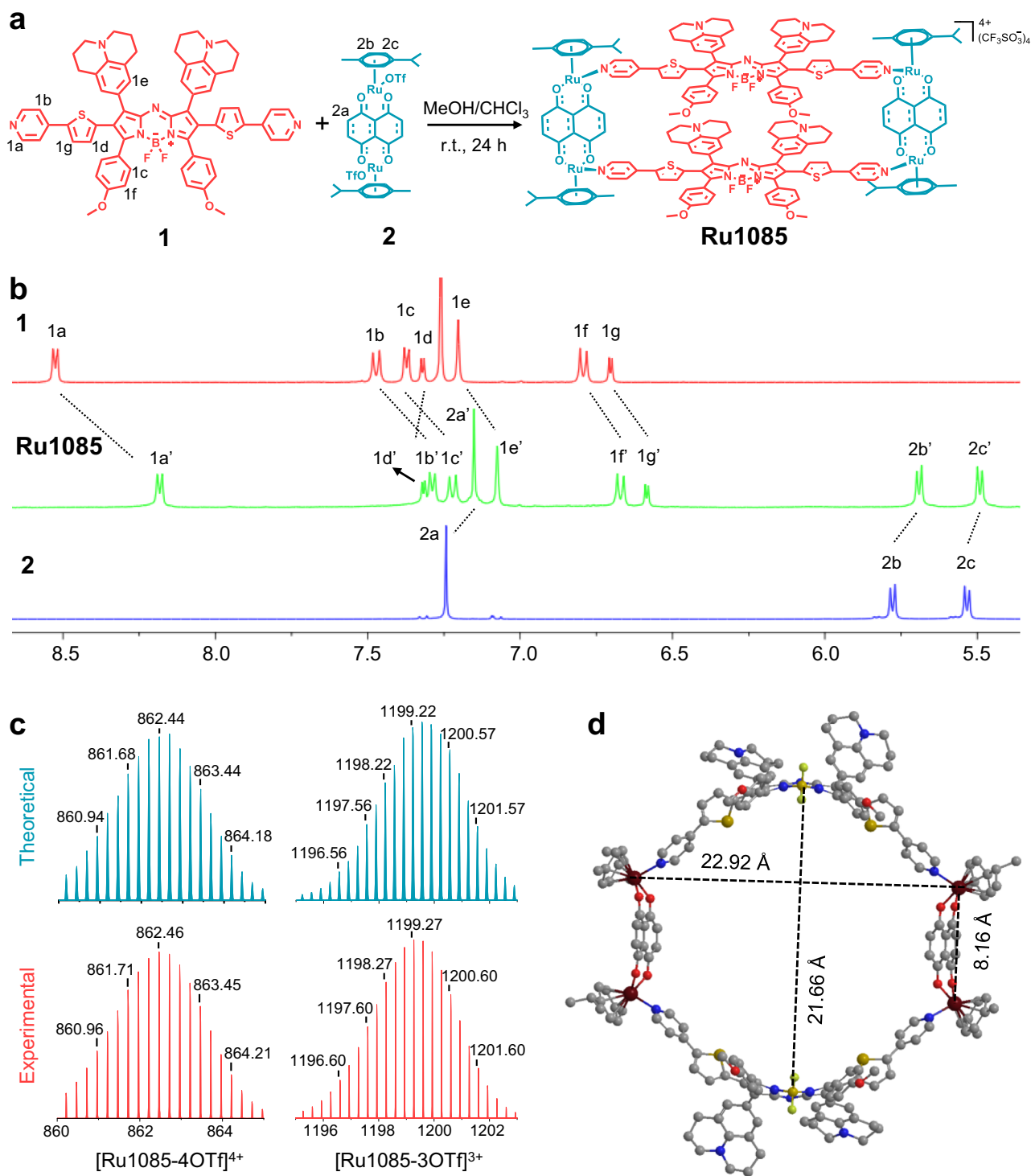


Fig. 2 Synthesis, characterization, and theoretical calculation of **Ru1085**. **a** Construction of ligand **1** with **2** to form **Ru1085**. **b** Partial ^1H NMR spectra of **1**, **Ru1085** and **2** (from top to bottom). **c** Theoretical (blue) and experimental (red) isotope patterns of $[\text{Ru1085-4OTf}]^{4+}$ (left) and $[\text{Ru1085-3OTf}]^{3+}$ (right) for ESI-TOF-MS. **d** Molecular model of **Ru1085** optimized by B3LYP molecular orbital approach.

In vitro antitumor activity and mechanism. The antitumor activity of was assessed against A549 (lung), Hela (cervix) and HepG2 (liver) tumor cell lines. $\text{Ru}(\text{bpy})_3\text{Cl}_2$, cisplatin and 5-ALA (5-aminolevulinic acid, clinically PDT agent) were chosen as comparisons (Table 1). **Ru1085** presented tremendous antitumor capability with high cytotoxicity values in above cell lines. With 808 nm laser illumination, enhanced cytotoxicity of **Ru1085** was found, especially in A549 cells ($\text{IC}_{50, \text{light}} = 4.5 \mu\text{M}$). The

phototoxic index (PI, defined as $\text{IC}_{50, \text{dark}}/\text{IC}_{50, \text{light}}$) of **Ru1085** in A549 cells could reach the highest value among examined cell lines. Hence, A549 cell line was selected for further exploration. Low or almost no cytotoxicity was found for 5-ALA and $\text{Ru}(\text{bpy})_3\text{Cl}_2$ (IC_{50} range from 87.4 to $>300 \mu\text{M}$).

Considering the hypoxic environment of solid tumor, the antitumor activity was estimated under hypoxia (1% O_2). Excitingly, no obvious decline in antitumor efficiency of

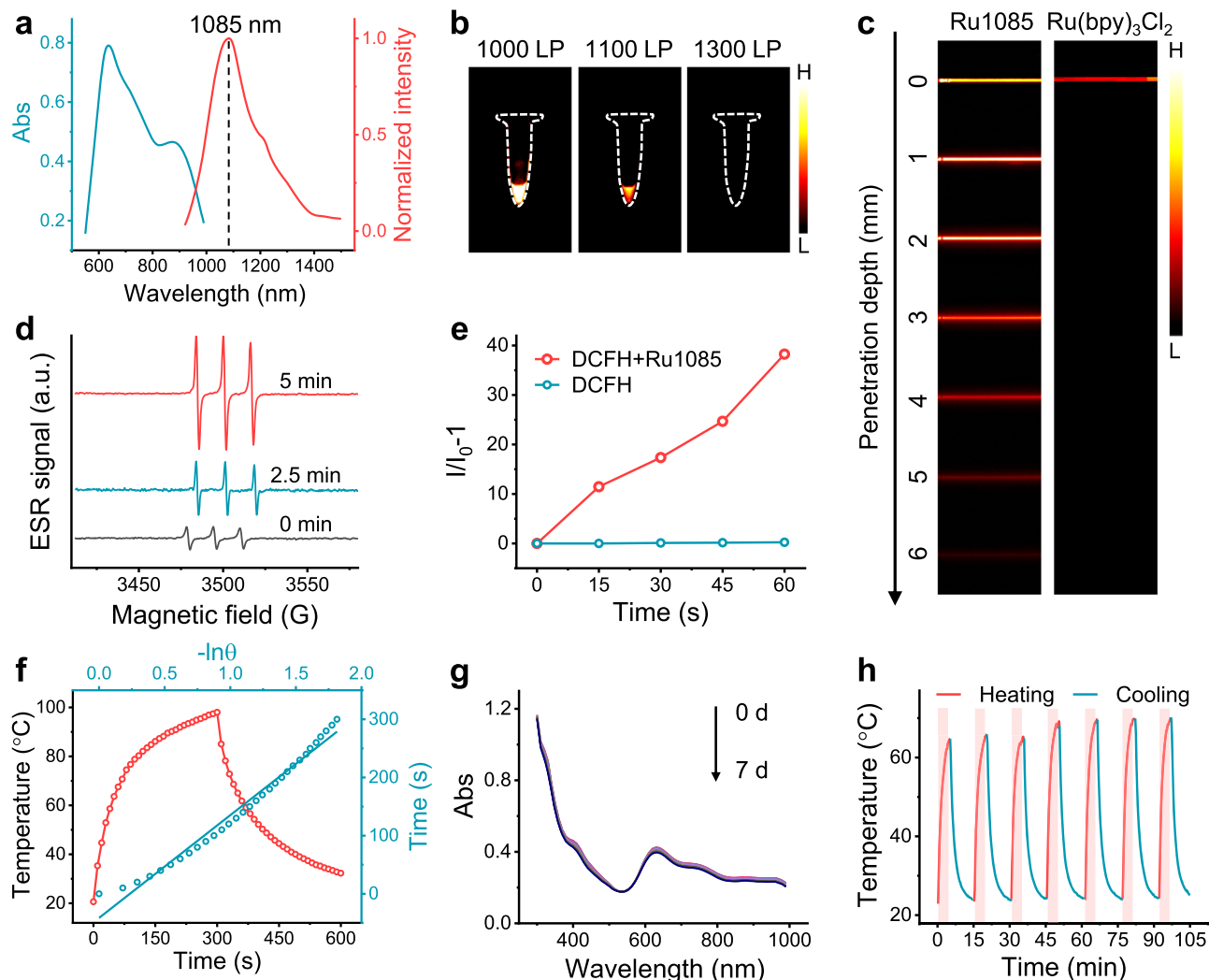


Fig. 3 In vitro photophysical, photodynamic, photothermal properties, and stability of Ru1085. **a** Absorption and normalized emission spectra ($\lambda_{\text{ex}} = 808 \text{ nm}$) of Ru1085 in DCM. **b** NIR-II fluorescence images of Ru1085 under different long-pass filters. **c** Fluorescence images of Ru1085 and Ru(bpy)₃Cl₂ encapsulated in capillaries and immersed at different depths in 1% intralipid. **d** Detection of ¹O₂ analyzed by ESR measurement. **e** ROS generation of Ru1085 (20 μM) illuminated by 808 nm laser (0.8 W cm⁻²) using H₂-DCFH as indicator. **f** Monitored temperature profile (red line) of Ru1085 illuminated for 300 s and followed by natural cooling, and linear time data versus $-\ln\theta$ (blue line) from the cooling period. **g** The stability tests of Ru1085 incubated in 10% FBS for 7 days. **h** Photothermal stability of Ru1085 (10 μM) illuminated by 808 nm laser (0.8 W cm⁻²) for seven repeating cycles of heating-cooling.

Ru1085 was observed when cells moved from normoxia ($\text{IC}_{50, \text{light}} = 4.5 \mu\text{M}$) to hypoxia (4.9 μM). We speculated that the photocytotoxicity of Ru1085 was not primarily dependent on ¹O₂. ROS scavenging tests proved the generation of very minor ¹O₂, and the produced ROS types mainly included hydroxyl radical (OH[•]), hydrogen peroxide (H₂O₂) and superoxide radical (O₂^{•-}) (Supplementary Fig. 20). On the contrary, the PDT agent 5-ALA presented much lower photocytotoxicity in hypoxia ($\text{IC}_{50, \text{light}} > 300 \mu\text{M}$) than that in normoxia (87.4 μM), indicating the antitumor efficiency of 5-ALA would dramatically reduce in solid tumor. Meanwhile, the activity of Ru1085 against drug-resistant tumor cells was investigated in cisplatin-resistant A549 cells (A549cisR). The resistant factor (RF) was defined as IC_{50} in A549/ IC_{50} in A549cisR. Promisingly, Ru1085 exhibited prominent antitumor activity in overcoming drug resistance with a high RF of 2.2, which was ~4-fold of that of cisplatin (RF = 0.5). Attractively, Ru1085 showed desirable selectivity in normal cells (16HBE cell line) with a high selectivity index (SI = 3.4), defined as IC_{50} in 16HBE/ IC_{50} in A549, while cisplatin was even more

toxic in normal cells (0.3). Therefore, these results showed that Ru1085 presented prominent antitumor capability and could be a candidate for further in vivo antitumor practice.

Inspired by the admirable cytotoxicity against malignant cells, the possible antitumor mechanism of Ru1085 was then investigated. First, considering Ru1085 mainly localized in lysosomes, the integrity of lysosomes was confirmed using acridine orange (AO) staining. Once lysosomes were damaged, the red fluorescence of AO would reduce. As depicted in Fig. 5a and Supplementary Fig. 21, the red fluorescence of AO almost disappeared, indicating that the lysosomes were dysfunctional after treated with Ru1085 and Ru1085 along with laser illumination. Moreover, Ru1085 also partially localized in mitochondria. Thus, 5,5',6,6'-tetrachloro-1,1',3,3'-tetraethylbenzimidazolylcarbocyanine iodide (JC-1), an indicator of the mitochondrial membrane potential (MMP), was employed to monitor the change of MMP. When MMP was reduced, the fluorescence of JC-1 could change from red to green. The green fluorescence indicated that Ru1085 could significantly induce

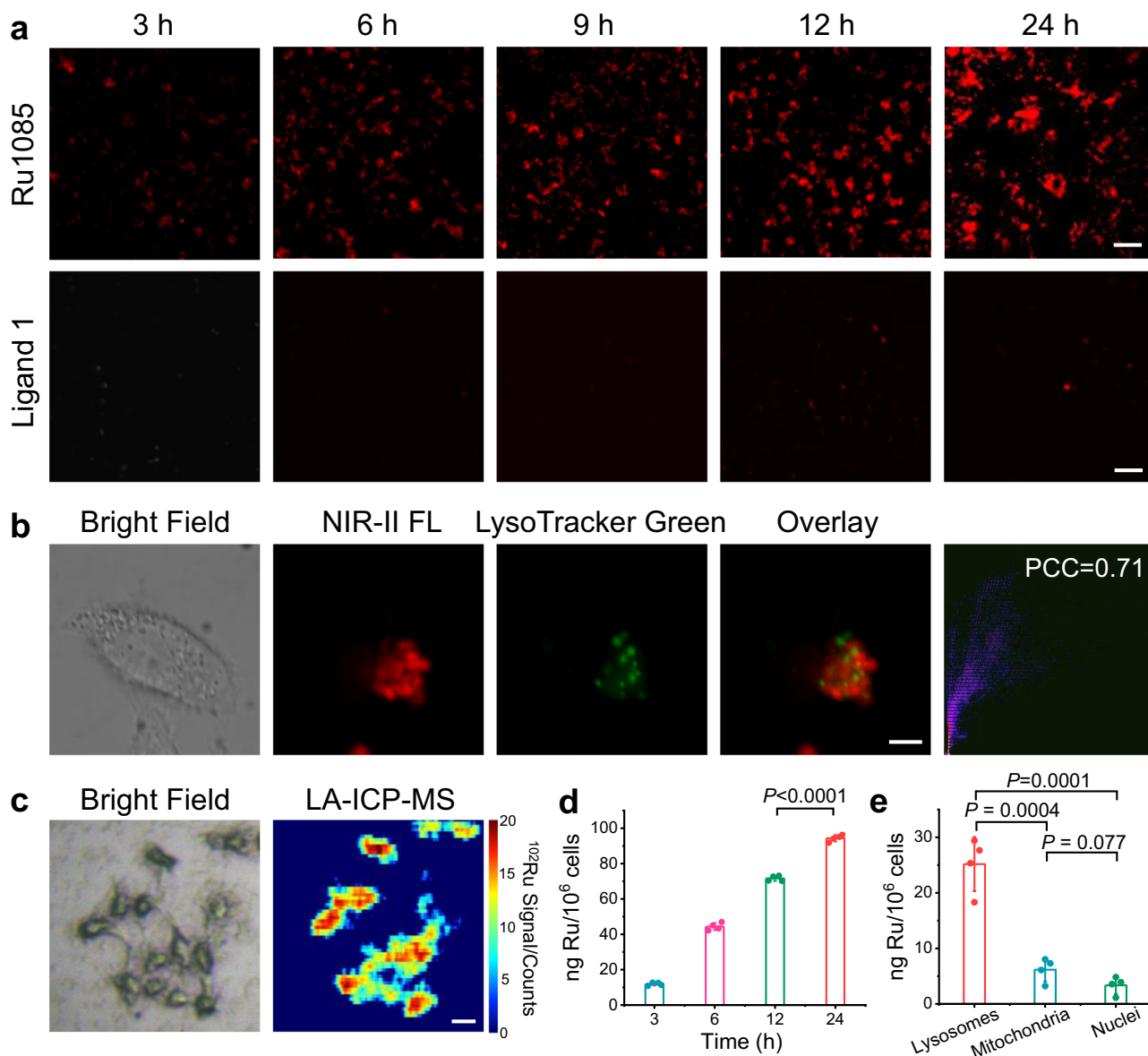


Fig. 4 Cellular uptake and localization of Ru1085 in A549 cells. **a** NIR-II fluorescence images of cells incubated with **Ru1085** (10 μM) and ligand **1** (20 μM) over time. Scale bar, 50 μm . **b** Colocalization assay of **Ru1085** (10 μM) using LysoTracker Green as lysosomal dye. The PCC was calculated to be 0.71. Scale bar, 5 μm . **c** LA-ICP-MS imaging of ^{102}Ru in cells after incubated with **Ru1085** (5 μM). Scale bar, 20 μm . ICP-MS results of **d** intracellular Ru amount with time-dependence and **e** Ru localization after incubated with **Ru1085** (5 μM) for 6 h. Data were presented as mean \pm s.d. ($n = 4$). Statistical differences were analyzed by Student's two-sided *t*-test. Source data are provided in Source Data file.

mitochondrial depolarization and the laser illumination further aggravated mitochondrial damage (Fig. 5b and Supplementary Fig. 22). Mitochondria are generally sensitive to toxic ROS, and oxidative stresses induced by ROS can cause mitochondrial membrane depolarization⁵². Therefore, ROS production was tested by the staining with $\text{H}_2\text{-DCFH}$, which could be deacetylated in cells and oxidized by ROS into DCF emitting green fluorescence. The DCF fluorescence remarkably increased after treated with **Ru1085** along with laser illumination (Fig. 5c), indicating ROS was generated in cells. Mitochondria damage often triggers the downstream caspase cascade activation and apoptosis. Hence, we evaluated the expression of caspase 3/7 and **Ru1085** efficiently activated caspase 3/7, especially in **Ru1085** along with laser group (Fig. 5d). In addition, caspase 1, as a member of the cysteine protease family, facilitates the activations of caspase 3/7⁵³. Furthermore, caspase 1 activity tests showed that

Ru1085 could activate caspase 1 (Fig. 5e). Given that active caspase 3/7 is an effector in apoptotic pathways, cell apoptosis was then investigated using Annexin V-FITC/propidium iodide (PI) double-staining. As shown in Fig. 5f, **Ru1085** mainly induced early apoptosis (AV + /PI -) and **Ru1085** along with laser illumination mainly caused late apoptosis/necrosis (AV + /PI +). Due to the nuclear accumulation of **Ru1085**, the influence for nucleus was further evaluated by analyzing cell cycle distribution. The cell cycle was mainly arrested at S and G2/M phase, suggesting the suppression of DNA replication and mitosis (Fig. 5g, h). In conclusion, the underlying antitumor mechanism of **Ru1085** was attributed to mitochondria-mediated apoptosis and cell cycle arrest at S and G2/M phase.

In addition to inhibiting malignant cell proliferation, the antimetastatic activity of **Ru1085** was explored because some Ru(II) complexes exhibited suppressing tumor metastasis in

Table 1 IC₅₀ value of Ru1085, Ru(bpy)₃Cl₂, cisplatin and 5-ALA against various cell lines by MTT assay.

Condition	Cell line	Dark/light ^a	IC ₅₀ (μM)				PI ^b	
			Ru1085	Ru(bpy) ₃ Cl ₂	Cisplatin	5-ALA		
Normoxia	A549	Dark	11.6 ± 1.8	>300	21.5 ± 0.1	>300	2.5	
		Light	4.5 ± 0.5	>300	-	87.4 ± 1.1		
	Hela	Dark	10.0 ± 2.9	>300	21.2 ± 2.0	>300	1.7	
		Light	5.9 ± 1.9	>300	-	168.0 ± 27.0		
	HepG2	Dark	21.2 ± 1.3	>300	9.1 ± 1.4	>300	1.5	
		Light	13.5 ± 4.2	>300	-	101.9 ± 13.9		
	A549cisR	Dark	5.3 ± 0.3	>300	44.7 ± 3.6	>300	1.4	
		Light	3.9 ± 0.4	>300	-	268.8 ± 16.0		
	16HBE	RFC ^c	Dark	2.2	-	0.5	-	1.1
			Light	39.4 ± 8.4	>300	5.5 ± 0.3	>300	
SI ^d			37.1 ± 12.9	>300	-	-		
Hypoxia	A549	Dark	3.4	-	0.3	-	1.7	
		Light	8.1 ± 1.4	>300	37.6 ± 1.2	>300		
		Light	4.9 ± 1.2	>300	-	>300		

^aThe light source used for Ru1085 was 808 nm laser and the light source used for Ru(bpy)₃Cl₂ and 5-ALA was 450 nm LED.
^bPI (phototoxic index) = IC_{50, dark} treated with Ru1085/IC_{50, light} treated with Ru1085.
^cRF (resistant factor) = IC_{50, dark} in A549/IC_{50, dark} in A549cisR.
^dSI (selectivity index) = IC_{50, dark} in 16HBE/IC_{50, dark} in A549.

previous reports^{54,55}. The wound-healing assay was performed to evaluate the anti-migration efficiency of Ru1085 (Supplementary Fig. 23). Attractively, only after treated with Ru1085 and Ru1085 along with laser illumination, the migration of cells was efficiently suppressed (wound closure ratio <7%). Afterwards, a transwell invasion assay was utilized to assess the anti-invasion potential of Ru1085 (Supplementary Fig. 24). The diminished invasion was observed after treated with Ru1085 and Ru1085 along with laser illumination with an invasion ratio of 45 and 25%, respectively. To sum up, the above data indicated that Ru1085 also significantly inhibited the migration and invasion of tumor cells.

In vivo NIR-II fluorescence imaging-guided and monitored tumor chemo-phototherapy. With above promising in vitro antitumor capability, the in vivo application of Ru1085 was further explored. To improve the tumor-targeting ability, Ru1085 was encapsulated into DSPE-PEG5000 (encapsulation rate *ca.* 31%, Supplementary Fig. 25). After encapsulation, the absorption and emission spectra of Ru1085 NPs had minimal shift compared with Ru1085 (Supplementary Fig. 26). PCE of Ru1085 NPs was calculated to be 36.7% (Supplementary Fig. 27). Dynamic light scattering (DLS) results suggested that the average diameter of Ru1085 NPs was ~220 nm in water, and the size obtained from transmission electron microscopy (TEM) imaging was ~170 nm (Supplementary Fig. 28). To determine the stability of Ru1085 NPs, the optical and size profiles in physiological condition were carried out. After incubated in 10% FBS or whole blood and storage for a whole week, the absorption spectra of Ru1085 NPs showed negligible change (Supplementary Fig. 29). Meanwhile, the size distribution had minimum change after incubated in PBS or 10% FBS (Supplementary Fig. 30). With continuous laser illumination, no significant change was observed in absorbance (Supplementary Fig. 31). Prior to intravenous injection, the biosafety of Ru1085 NPs was investigated by performing hemolysis assay (Supplementary Fig. 32). Ru1085 NPs exhibited no hemolysis at various concentration (5–120 μM), which can be attributed to the encapsulation of Ru1085 by liposome. These data verified the stability and biosafety of Ru1085 NPs, which enabled the further in vivo application.

To estimate the in vivo NIR-II fluorescence performance of Ru1085 NPs, we carried out NIR-II fluorescence imaging of the

regional vascular system of hindlimb. The arteries and veins could be clearly visualized from the background skin tissue with excellent signal to background ratio (SBR = 13.6) and ideal spatial resolution (narrow full width at half-maximum (FWHM) = 424 μm) (Fig. 6a, b). In contrast, the vessels could not be distinguished from skin using Ru(bpy)₃Cl₂ NPs as probe, confirming the drawbacks of short wavelength (Supplementary Fig. 33). In light of the successful in vivo NIR-II fluorescence imaging of Ru1085 NPs, A549 tumor-bearing mice models were established. We employed ICP-MS to evaluate pharmacokinetics by quantifying Ru amounts in plasma after injection and Ru1085 NPs exhibited a prolonged circulation time in blood (Fig. 6c). Meanwhile, the NIR-II fluorescence imaging was collected at various time points post-injection, and the signal in tumor was gradually enhanced and reached the highest value at 24 h post-injection of Ru1085 NPs with a high SBR of 6.6 (Fig. 6d and Supplementary Fig. 34). Tumors and other organs were collected at 24 h post-injection for analysis of the NIR-II fluorescence intensity, illustrating the successful tumor accumulation (Supplementary Fig. 35).

Under the guidance of NIR-II fluorescence imaging, the synergistic therapeutic effect was then explored. A459 xenograft tumor models were randomly divided into five groups (*n* = 5/group) and intravenously injected with Ru1085 NPs (1 mg Ru/kg), cisplatin (1 mg Pt/kg), or PBS (10 mM). The tumors were subjected with or without 808 nm laser illumination at 24 h post-injection. The photothermal images and temperature elevation were recorded by an infrared thermal camera (Fig. 6e and Supplementary Fig. 36). The temperature of tumor in Ru1085 NPs along with laser illumination group reached 54.1 °C. Besides, the ROS generation in tumors was tested using dihydroethidium (DHE, a ROS indicator) staining. Strong fluorescence was observed in Ru1085 NPs along with laser illumination group, indicating ROS production in tumor after phototherapy (Fig. 6f).

Furthermore, NIR-II fluorescence imaging was performed for real-time monitoring the tumor lesion and depicting tumor margin with high SBR (SBR >4, 12–120 h) during the chemo-phototherapy period (Fig. 6g and Supplementary Fig. 37). To compare therapeutic effect of different groups, the tumor volume was recorded every other day (Fig. 6h and Supplementary Fig. 38). In Ru1085 NPs and cisplatin group, the tumor growth was under suppression at the beginning of chemotherapy, but severely recurred on the eighth day, suggesting that the single

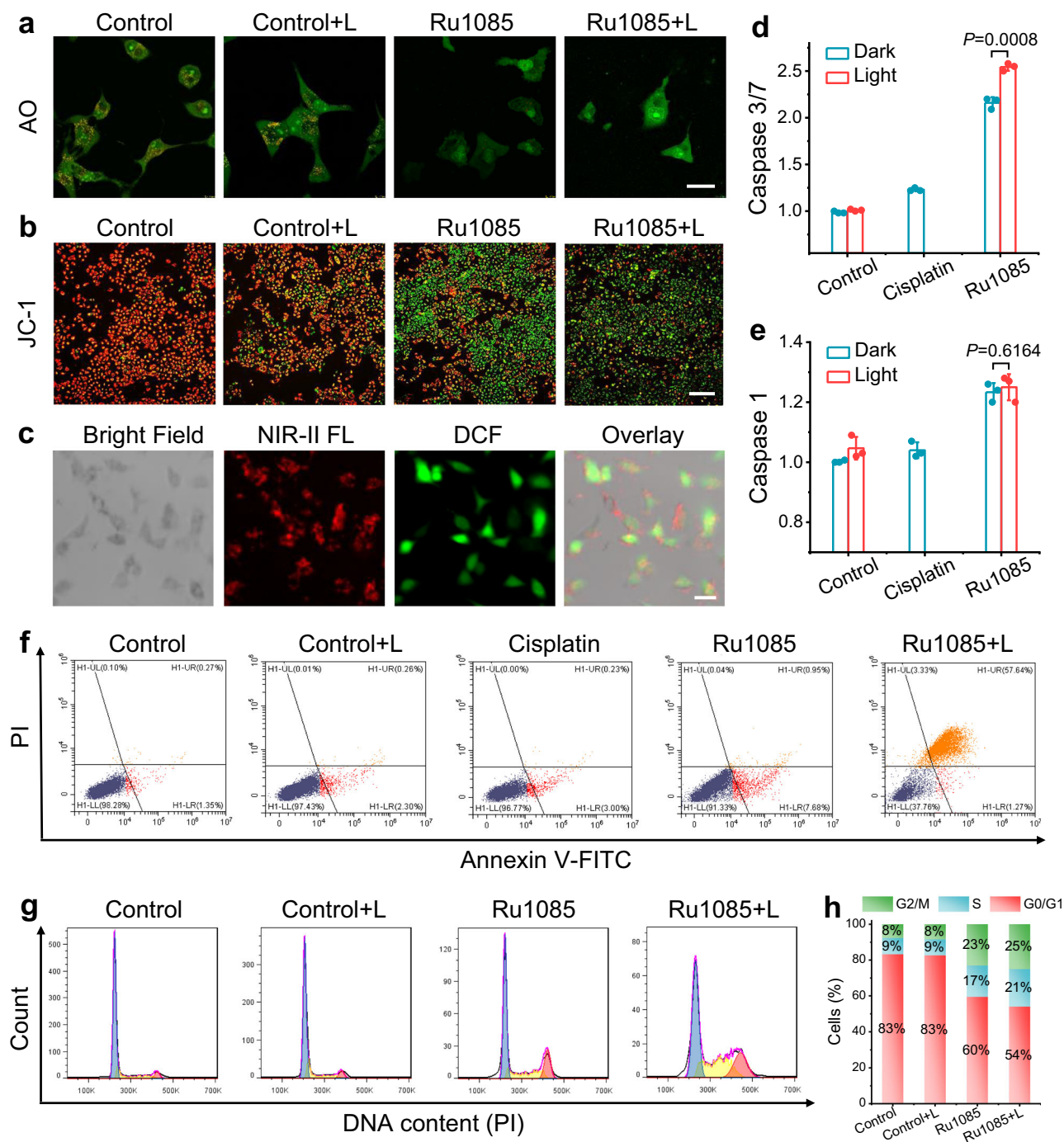


Fig. 5 Antitumor mechanism of Ru1085 in A549 cells. After incubated with **Ru1085** (10 μM) or serum-free medium and treated with or without 808 nm laser illumination (0.8 W cm^{-2} , 5 min), cells were taken **a** AO and **b** JC-1 staining. Scale bars, **a**: 20 μm ; **b**: 300 μm . **c** $\text{H}_2\text{-DCFH}$ staining of cells treated with **Ru1085** along with laser illumination. Scale bar, 20 μm . Relative caspase 3/7 (**d**) and caspase 1 (**e**) activity after various treatments ($n = 3$). **f** Flow cytometer results of Annexin V-FITC/PI double-stained cells after various treatments. **g** Cell cycle analysis of cells after various treatments. **h** Histogram depicting of the cell population distribution in cell cycle phase in (**g**). Data were presented as mean \pm s.d. ($n = 3$). Statistical differences were analyzed by Student's two-sided t -test. Source data are provided in Source Data file.

chemotherapy could not eradicate tumor. Only in chemo-phototherapy group which was administrated with **Ru1085** NPs along with laser illumination, the tumor was successfully suppressed and almost no recurrence was detected. Histological staining of the tumors in each group showed that the severe cellular necrosis was only found in chemo-phototherapy group (Supplementary Fig. 39), supporting the therapeutic effect as mentioned. Negligible body weight loss was found after

therapeutic period (Fig. 6i). Notably, the body weight of cisplatin group obviously declined (from $18.5 \pm 0.6 \text{ g}$ to $17.7 \pm 0.9 \text{ g}$) during the first four days, indicating the potential toxicity of cisplatin. Further histological staining of major organs and blood biochemical parameters revealed that no tissue damage and no abnormality in hepatorenal function after administration of **Ru1085** NPs (Supplementary Figs. 40, 41), which suggested negligible long-term systemic toxicity was introduced by **Ru1085**

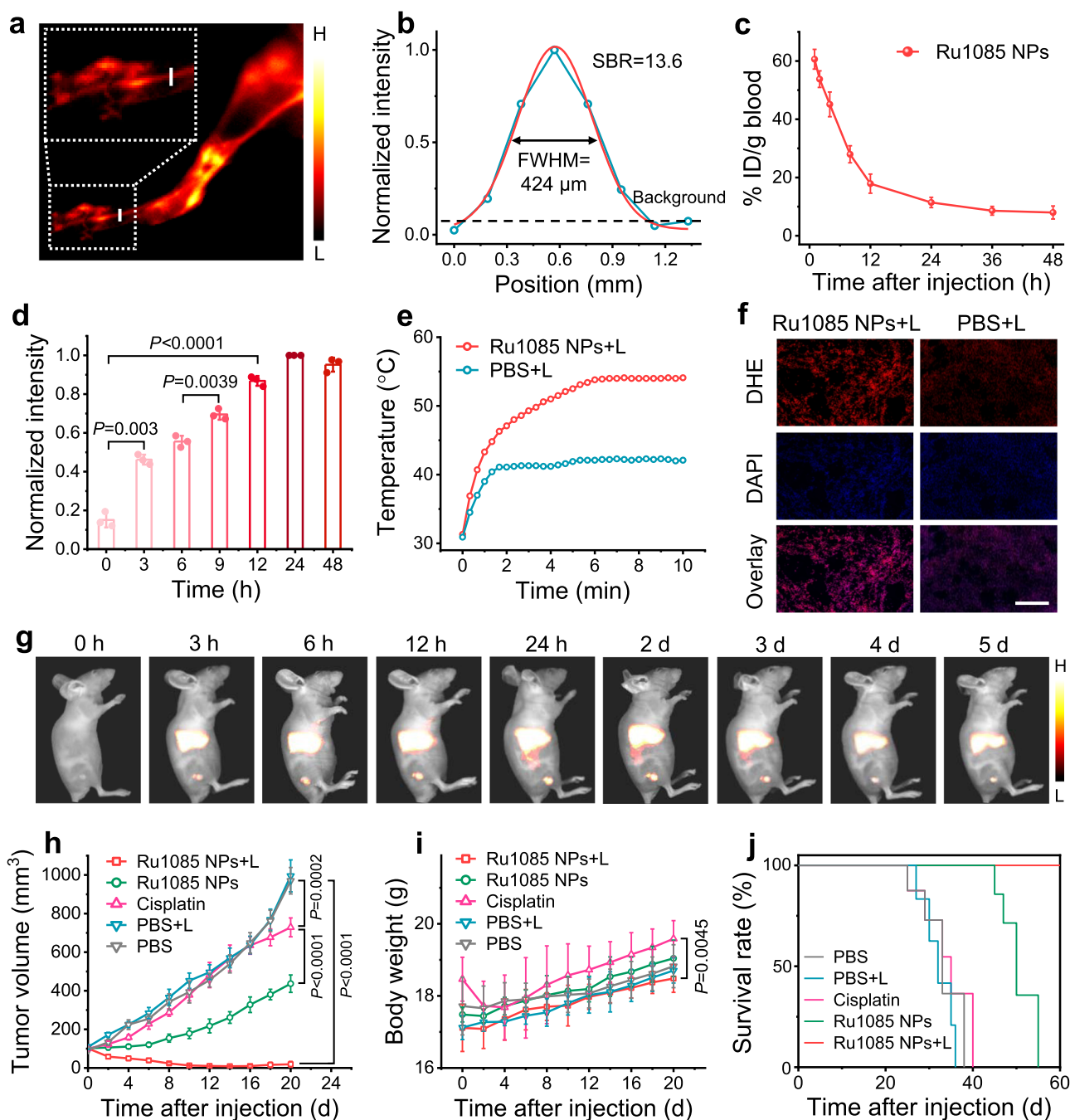


Fig. 6 In vivo NIR-II fluorescence imaging and chemo-phototherapeutic effect of Ru1085 NPs in A549 tumor-bearing mice. **a** NIR-II fluorescence images of hindlimb vessels after intravenous injection of Ru1085 NPs. **b** NIR-II fluorescence intensity profiles (blue line) and Gaussian fit (red line) along the white full line in (a). **c** Blood retention and **d** analysis of NIR-II fluorescence signals in tumor regions after injection of Ru1085 NPs. Data were presented as mean \pm s.d. ($n = 3$ independent mice). **e** Temperature change in tumor region with 808 nm laser illumination (0.8 W cm^{-2} , 10 min) at 24 h post-injection of Ru1085 NPs or PBS. **f** DHE and DAPI staining of tumor slices. Scale bar, 400 μm . **g** In vivo NIR-II fluorescence images of tumor models after injection of Ru1085 NPs. **h** Tumor inhibitory effect and **i** mice body weight of tumor models within 20 days of treatment. **j** Kaplan-Meier survival plots for various treated mice (Ru1085 NPs dose: 1 mg Ru/kg, cisplatin dose: 1 mg Pt/kg, laser treatments: 0.8 W cm^{-2} for 10 min). Data were presented as mean \pm s.d. ($n = 5$ independent mice). Statistical differences were analyzed by Student's two-sided *t*-test. Source data are provided in Source Data file.

NPs. To further assess the therapeutic effect, the life-time of mice models after various treatments was recorded. The chemo-phototherapy could significantly prolong the survival time to over 60 days (Fig. 6j). All these data specified that Ru1085 NPs inherent with biosafety successfully accomplished high-resolution NIR-II fluorescence imaging, guided chemo-phototherapy with enhanced performance, and monitored the therapeutic response.

Discussion

Most existing Ru-based agents suffered from short excitation/emission wavelength and the corresponding excitation light failed to penetrate deep into the tissues in phototherapy. Herein, we successfully designed a metallacycle Ru1085 which was excited at 808 nm and emitted over 1000 nm. The 808 nm laser can penetrate deeper tissues ($\sim 6 \text{ mm}$) compared with the short-wavelength

light source (<600 nm) that was employed for Ru complexes in previous reports^{12,56}.

Ru1085 exhibited much more efficient uptake in cells than ligand **1**, which could be attributed to the higher lipophilicity⁴⁴, positive charge⁵⁷, and characteristic ring tension⁵⁸ of metallacycle. Further studies suggested the endocytic uptake mechanism and **Ru1085** mainly localized in lysosomes along with partially enriched in mitochondria and nucleus. The positive-charge and lipophilicity of **Ru1085** could result in the localization in mitochondria and nucleus^{48,59}, which facilitated toxic ROS inducing cell death considering mitochondria and nucleus are sensitive to ROS⁶⁰.

Afterwards, the *in vitro* antitumor performance of **Ru1085** was evaluated in details. First, **Ru1085** presented higher dark/photo-cytotoxicity in various tumor cell lines than Ru(bpy)₃Cl₂ and 5-ALA, especially in A549 cell line. Second, compared with the significant photocytotoxicity decrease of clinical photosensitizer 5-ALA during the transfer of cells from normoxia to hypoxia, the antitumor efficiency of **Ru1085** had almost no change regardless of cells in normoxia or in hypoxia. Last, **Ru1085** was capable of overcoming cisplatin resistance and possessed selectivity between cancer cells and normal cells. It is anticipated that further improvements could be realized by optimizing the PI value based on the strategy of increasing photocytotoxicity and reducing dark cytotoxicity simultaneously. For enhancing SI value, special peptides⁶¹ could be introduced into the skeleton to increase the specific uptake of tumor cells. Mechanistic studies revealed that **Ru1085** induced mitochondria-mediated apoptosis as well as S and G2/M phase cell cycle arrest. The exploration of antitumor mechanism of **Ru1085** helps us understand the cell death process of the synergistic therapy and provides first-hand information for rationally designing Ru-based metallacycle.

Further *in vivo* studies demonstrated the advantages of long excitation/emission wavelength of **Ru1085**. Notably, the precise profile of blood vessels with high SBR (over 10) and desirable spatial resolution (FWHM was at micron-level) was accomplished by the NIR-II fluorescence imaging. In xenografted tumor models, the NIR-II fluorescence imaging was able to guide the synergistic therapy and delineate the tumor change in real-time with precise tumor margin during the therapy period, which also provided essential imaging data for long-term assessing the therapeutic effect. Herein, through one treatment of single dose of **Ru1085** NPs along with single laser illumination, the theranostics was achieved and the synergistic therapy was more efficient than single therapy. Therefore, the construction of long-wavelength emissive metal-based agents could enhance optical penetration for improving phototherapeutic efficacy in deep and/or solid tumors. Besides, taking the intrinsic advantage of long-wavelength emission, they could be utilized as a universal platform for visualizing the delivery, targeting, pharmacokinetics, and distribution through fluorescence imaging. Finally, such a system could provide real-time feedback to the treatment, and facilitate the clinic translation of metal agents in synergistic chemo-phototherapy in the future.

In summary, we have constructed a novel Ru(II) metallacycle (**Ru1085**) emitting over 1000 nm and achieved precise NIR-II fluorescence imaging-guided and monitored chemo-phototherapy. By introducing aza-BODIPY (**1**) as an NIR-II fluorescence emitter into the Ru(II) metallacycle skeleton, the emission peak of **Ru1085** was shifted into NIR-II biowindow compared with traditional Ru complexes, and the optical penetration depth reached up to 6 mm, facilitating NIR-II fluorescence imaging with high spatial-temporal resolution and efficient phototherapy. The anticancer capability of **Ru1085** was prominent in a cisplatin-resistant cell line with low toxicity on normal cells. Through one treatment, **Ru1085** could be successfully utilized in NIR-II fluorescence imaging-guided chemo-

phototherapy and monitored long-term therapeutic response in tumor models. This work proposed a novel strategy to develop an emitted over 1000 nm metallacycle, which provided promising opportunities for metal-based agents applied in biomedicine.

Methods

Synthesis and characterization of Ru1085. To synthesize **Ru1085**, **1** (5.20 mg, 0.00488 mmol) and **2** (4.82 mg, 0.00488 mmol) were dissolved in a mixture of MeOH (4 mL) and CHCl₃ (4 mL) in a glass vial. After stirring at room temperature for 24 h, the assembled product was concentrated by rotary evaporation, precipitated by addition of diethyl ether, and washed three times with diethyl ether followed by dried under vacuum to afford green solids of **Ru1085** (7.30 mg, yield 72%). Structural characterization was determined by ¹H NMR, ¹⁹F NMR, 2D rotating frame Overhauser effect spectroscopy (ROESY), and electrospray ionization time-of-flight mass spectrometry (ESI-TOF-MS).

Calculation of NIR-II fluorescence quantum yield (Φ_f). The NIR-II fluorescence quantum yield (Φ_f) was measured using a relative strategy. The Φ_f was calculated using IR-26 (Φ_f = 0.1%) as reference according to the following formula:

$$\Phi_{f(X)} = \Phi_{f(\text{ref})} \times \frac{S_X}{S_{\text{ref}}} \times \left(\frac{n_{\text{ref}}}{n_X} \right)^2 \quad (1)$$

where subscripts X and ref designate **Ru1085** and IR-26, respectively. S stands for the slope obtained by linear fitting of the integrated emission spectrum against the absorbance at 808 nm, and n stands for the refractive indices of their respective solvents.

Tissue phantom imaging study. 1% intralipid was used to simulate tissue due to its similar scattering features. Glass capillaries were filled with **Ru1085** and Ru(bpy)₃Cl₂, and then covered with various volumes of intralipid in a dish for imaging. The fluorescence images were then obtained by using 808 nm laser illumination for **Ru1085**, and 460 nm laser illumination for Ru(bpy)₃Cl₂.

Assessment of ¹O₂ generation. ESR analysis was performed to monitor the generation of ¹O₂. ESR spectra of **Ru1085** solution (5 μM) containing TEMP (300 mM) were obtained by using 808 nm laser illumination (0.8 W cm⁻²) with various illumination time.

The evaluation of ¹O₂ quantum yield (Φ_Δ) used DPBF as probe via UV-Vis spectroscopy. The working samples containing DPBF (20 μg mL⁻¹) and **Ru1085** solution (20 μM) or ICG (20 μM) were irradiated with 808 nm laser (0.8 W cm⁻²) for various time. The Φ_Δ was calculated using ICG (Φ_Δ = 0.2) as reference according to the following formula:

$$\Phi_{\Delta(X)} = \Phi_{\Delta(\text{ref})} \times \frac{S_X}{S_{\text{ref}}} \times \frac{F_{\text{ref}}}{F_X} \quad (2)$$

where subscripts X and ref designate **Ru1085** and ICG, respectively. S stands for the slope of plot of the absorbance of DPBF (at 405 nm), and F stands for the absorption correction factor ($F = 1 - 10^{-\text{OD}_{808}}$).

Assessment of ROS generation. H₂-DCFH (1.0 mM, 0.8 mL) in DMSO was mixed with NaOH (0.01 M, 2 mL) to deacetylate into DCFH. Added the prepared DCFH (20 μM) into **Ru1085** solution (20 μM) and then irradiated with 808 nm laser for 0, 30, 60, 90, and 120 s. The fluorescent spectra of DCF (λ_{ex} = 488 nm, λ_{em} = 525 nm) were recorded.

Photothermal properties and the photothermal conversion efficiency (PCE) of Ru1085. **Ru1085** solution (0, 2.5, 5, 7.5, and 10 μM) was irradiated with 808 nm laser (0.8 W cm⁻²) for 5 min, and was recorded by an infrared thermal imaging camera. The photothermal conversion efficiency (PCE) of **Ru1085** was calculated according to the following formula, in which T_{max} (or T_{sur}) is the equilibrium temperature (or ambient temperature), I is the incident laser power (I = 0.8 W cm⁻²), A₈₀₈ is the absorbance at 808 nm, and τ_s is the system time constant of the sample.

$$\text{PCE} = \frac{hs(T_{\text{max}} - T_{\text{sur}}) - Q_0}{I(1 - 10^{-A_{808}})} \quad (3)$$

$$hs = \frac{\sum_i m_i C_{p,i}}{\tau_s} \quad (4)$$

$$\tau_s = \frac{t}{-\ln \theta} = \frac{t}{-\ln \left(\frac{T - T_{\text{sur}}}{T_{\text{max}} - T_{\text{sur}}} \right)} \quad (5)$$

Stability tests of Ru1085. For chemical-stability tests, **Ru1085** (50 μM) was incubated in PBS or 10% FBS and stored for a whole week. The UV-Vis absorption of **Ru1085** was measured every day. The photostability of **Ru1085** was investigated

by recording the absorption spectra, for which the UV-Vis absorption of **Ru1085** (50 μM) was measured after 808 nm laser illumination (0.4 W cm^{-2}) for various time (0, 10, 20, 30 min). For photothermal stability tests, **Ru1085** (10 μM) was illuminated with 808 nm laser (0.8 W cm^{-2}) for 5 min and then naturally cooled for 10 min. The temperatures of seven heating-cooling cycles were recorded using an infrared thermal imaging camera.

Measurement of octanol/water partition coefficient ($\log P_{o/w}$). Utilizing the “shake-flask” method to detect the distribution coefficient between water and octanol phase. The used phases were saturated in each other at first. Then **Ru1085** and ligand **1** were dissolved in phase A. This solution was subsequently mixed with an equal volume of phase B for 24 h using a mixer. Phase A was then carefully separated from phase B. The concentrations of **Ru1085** and **1** were determined by UV-Vis spectroscopy using the extinction coefficients of the complexes in water saturated with octanol. The $\log P_{o/w}$ value was calculated according to the following formula:

$$\log P_{o/w} = \log c[X]_{\text{oct}} - \log c[X]_{\text{PBS}} \quad (6)$$

Cellular uptake by fluorescence imaging. A549 cells were seeded on confocal dishes ($\sim 5 \times 10^4$ cells/dish). After incubated with **Ru1085** (10 μM) and ligand **1** (20 μM) for various time, A549 cells were washed three times and subjected for imaging by utilizing an NIR-II fluorescence microscope ($\lambda_{\text{ex}} = 808 \text{ nm}$, $\lambda_{\text{em}} = 1000\text{--}1200 \text{ nm}$).

Intracellular colocalization by fluorescence imaging. A549 cells were incubated with **Ru1085** (10 μM) for 6 h and then further incubated with LysoTracker Green (200 nM, 1 h), MitoTracker Deep Red (75 nM, 45 min), and Hoechst 33342 (5 $\mu\text{g mL}^{-1}$, 20 min), respectively. After washed three times by PBS, cells were visualized by a fluorescence microscope. Fluorescence images were collected in the following channels: LysoTracker Green ($\lambda_{\text{ex}} = 488 \text{ nm}$, $\lambda_{\text{em}} = 520\text{--}550 \text{ nm}$); MitoTracker Deep Red ($\lambda_{\text{ex}} = 644 \text{ nm}$, $\lambda_{\text{em}} = 665\text{--}700 \text{ nm}$); Hoechst 33342 ($\lambda_{\text{ex}} = 405 \text{ nm}$, $\lambda_{\text{em}} = 430\text{--}460 \text{ nm}$); **Ru1085** ($\lambda_{\text{ex}} = 808 \text{ nm}$, $\lambda_{\text{em}} = 1000\text{--}1200 \text{ nm}$). Pearson correlation coefficient was quantified using ImageJ.

Elemental imaging by LA-ICP-MS. A549 cells were seeded in 24-well culture plates with cell climbing slices for overnight and then incubated with **Ru1085** (5 μM) for 6 h. After washed by PBS w/o Ca/Mg, cells were fixed with 70% cold alcohol solution and washed by water. Then, cells were allowed to adhere on slides to prepare LA-ICP-MS test. A laser spot size of 3 μm diameter, 10 μs^{-1} scan speed, 100 Hz repetition frequency, and laser fluence of $\sim 3 \text{ J cm}^{-2}$ were utilized to perform the test. ICP-MS parameters were as follows: radio frequency power of 1500 W, nebulizer gas flow of 1.25 L min^{-1} , auxiliary gas flow of 1.2 L min^{-1} , and plasma gas flow of 15 L min^{-1} . The monitored isotope ^{102}Ru was measured in counting mode. Images integration was performed by the software Igor-based Iolite V3.6.

Cellular uptake and localization by ICP-MS. For cellular uptake tests, A549 cells were incubated with **Ru1085** (5 μM) for various time (3, 6, 12, and 24 h) and then harvested for accurate cell counting. After digested using 60% HNO_3 , the samples were diluted to make the concentration of HNO_3 to 2%. The Ru content was determined by ICP-MS associated with the total cell numbers.

For cellular localization tests, A549 cells were incubated with **Ru1085** (5 μM) for 6 h and then harvested for accurate cell counting and equally separating into three parts. Each part was proceeded according to the protocol of lysosomal/mitochondria/nucleus extraction kit. Following process was conducted as above mentioned to determine the Ru content in various organelles.

Mechanism studies of cellular uptake. A549 cells were seeded on confocal dishes ($\sim 5 \times 10^4$ cells/dish). Cells were divided into six groups and pretreated with (1) **Ru1085** (10 μM) at 37 $^\circ\text{C}$; (2) **Ru1085** (10 μM) at 4 $^\circ\text{C}$; (3) **Ru1085** (10 μM) containing 2-Deoxy-D-glucose (50 mM) and oligomycin (5 μM) at 37 $^\circ\text{C}$; (4) **Ru1085** (10 μM) containing NH_4Cl (50 mM) at 37 $^\circ\text{C}$; (5) **Ru1085** (10 μM) containing sucrose (5 μM) at 37 $^\circ\text{C}$; and (6) **Ru1085** (10 μM) containing M- β CD (10 mM) at 37 $^\circ\text{C}$ for 1 h, respectively. After washed three times by PBS, cells were further incubated solely with **Ru1085** (10 μM) for another 5 h at 37 $^\circ\text{C}$. All cells were then washed with PBS for three times and subjected to NIR-II fluorescence.

In vitro cytotoxicity studies. The examined cell lines were seeded in 96-well plates ($\sim 5 \times 10^3$ cells/well). Cells were incubated with **Ru1085**, $\text{Ru}(\text{bpy})_3\text{Cl}_2$, cisplatin or 5-ALA at various concentrations for 12 h. The medium was replaced with fresh medium and cells were treated with or without light illumination. For incubation with **Ru1085**, cells were treated with 808 nm laser (0.8 W cm^{-2} , 5 min); for incubation with $\text{Ru}(\text{bpy})_3\text{Cl}_2$ or 5-ALA, cells were treated with a 450 nm LED (20 mW cm^{-2} , 5 min). After incubation for another 36 h, MTT assay was conducted according to the protocol.

Lysosomal disruption assay. A549 cells were seeded on confocal dishes ($\sim 5 \times 10^4$ cells/dish). After cells were incubated with **Ru1085** (10 μM) or serum-free medium for 12 h, the medium was replaced with fresh medium and cells were treated with or without 808 nm laser illumination (0.8 W cm^{-2} , 5 min). After further incubated for 12 h, cells were stained with AO (5 μM , 20 min), and subsequently visualized by an invert fluorescence microscope ($\lambda_{\text{ex}} = 488 \text{ nm}$, $\lambda_{\text{em}} = 520\text{--}550 \text{ nm}$ for green channel and 590–610 nm for red channel).

Mitochondrial membrane potential (MMP) assay. A549 cells were treated as above and stained with JC-1 (10 $\mu\text{g mL}^{-1}$, 20 min), and subsequently visualized by an invert fluorescence microscope ($\lambda_{\text{ex}} = 488 \text{ nm}$, $\lambda_{\text{em}} = 520\text{--}550 \text{ nm}$ for JC-1 monomer; $\lambda_{\text{ex}} = 530 \text{ nm}$, $\lambda_{\text{em}} = 590\text{--}610 \text{ nm}$ for JC-1 aggregate).

Detection of intracellular ROS generation. A549 cells were seeded on confocal dishes ($\sim 5 \times 10^4$ cells/dish). After cells were incubated with **Ru1085** (10 μM) for 6 h, the medium was replaced by $\text{H}_2\text{-DCFH}$ (20 μM) for further incubation (20 min). Then the medium was replaced with fresh medium, and cells were illuminated with 808 nm laser (0.4 W cm^{-2}) for 5 min and subsequently visualized by an invert fluorescence microscope ($\lambda_{\text{ex}} = 488 \text{ nm}$; $\lambda_{\text{em}} = 520\text{--}550 \text{ nm}$).

Scavenging intracellular ROS generation. A549 cells were seeded into 24-well plates (3×10^5 cells/well). After cells were incubated with **Ru1085** (10 μM) for 4 h, the cells were co-incubated with various ROS scavengers for another 2 h. The ROS scavengers included sodium pyruvate (10 mM), D-mannitol (50 mM), tiron (4,5-Dihydroxy-1,3-benzenedisulfonic acid disodium salt monohydrate, 5 mM), ebselen (2-Phenyl-1,2-benzisoselenazol-3(2H)-one, 50 μM), and sodium azide (50 μM), which were used to scavenge the generated hydrogen peroxide (H_2O_2), hydroxyl radical (OH^\bullet), superoxide radical ($\text{O}_2^{\bullet-}$), peroxynitrite anion (ONOO^-), and $^1\text{O}_2$, respectively. Then the cells were incubated with $\text{H}_2\text{-DCFH}$ (20 μM) for another 20 min. After that, the medium was replaced with fresh medium, and cells were illuminated with 808 nm laser (0.4 W cm^{-2}) for 5 min and subsequently visualized by an invert fluorescence microscope ($\lambda_{\text{ex}} = 488 \text{ nm}$; $\lambda_{\text{em}} = 520\text{--}550 \text{ nm}$).

Activation of caspase 3/7 and caspase 1. A549 cells were treated with serum-free medium (negative control), cisplatin (10 μM), or **Ru1085** (10 μM), respectively. After cells were incubated for 6 h, the medium was replaced with fresh medium, and cells were treated with or without 808 nm laser illumination (0.8 W cm^{-2} , 5 min). After further incubated for another 12 h, then cells were treated with caspase 3/7 or caspase 1 activity kit according to the manufacturer’s protocol.

Apoptosis and cell cycle analyses. For apoptosis tests, A549 cells were incubated with **Ru1085** (10 μM) or serum-free medium for 12 h, and then treated with or without 808 nm laser illumination (0.8 W cm^{-2}) for 5 min. After incubation for another 12 h, cells were stained with Annexin V-FITC and PI for 15 min and analyzed with flow cytometry.

For cell cycle analysis, A549 cells were treated as above and then lysed by RNase A (100 $\mu\text{g mL}^{-1}$) for 20 min. After that, cells were stained with PI (0.1 mg mL^{-1}) for 15 min and subsequently analyzed cell cycle distribution by flow cytometry.

Migration and invasion inhibition. The anti-migration ability was performed by wound-healing assay. A549 cells were seeded into 24-well plates (3×10^5 cells/well). Cells were incubated with **Ru1085** (10 μM) or serum-free medium for 12 h and then treated with or without laser illumination (808 nm, 0.8 W cm^{-2}) for 5 min. Horizontal lines were drawn using micro pipette tips in each well, and subsequently the wound was created. After further incubation for 12 and 24 h, cells were imaged by an invert fluorescence microscope with calcein-AM (5 μM) staining ($\lambda_{\text{ex}} = 488 \text{ nm}$; $\lambda_{\text{em}} = 520\text{--}550 \text{ nm}$). The wounds area was measured by ImageJ, and wound closure ratio was defined as $[1 - (\text{wound area at } t / \text{original wound area})] \times 100\%$. The anti-invasion capability was tested by Transwell/Matrigel invasion assay. Transwell inserts were pretreated with Matrigel (200 $\mu\text{g mL}^{-1}$, 100 $\mu\text{L/well}$). A549 cells were harvested and resuspended in **Ru1085** (10 μM) or serum-free medium, and subsequently added to upper chambers. The upper chambers were placed into the receiver wells, which were supplemented with complete medium. After further incubated for 48 h, the invaded cells were fixed with 4% paraformaldehyde, and washed with PBS and then stained with crystal violet. Transwell inserts visualization was performed on an invert fluorescence microscope. Cell invasion ratios were calculated according to OD_{590} .

Preparation of Ru1085 NPs. **Ru1085** (1 mg in acetonitrile) and DSPE-PEG5000 (9 mg in secondary water) were stirred overnight. After removing acetonitrile away using nitrogen gas, the mixture was centrifuged (3000 rpm) for 20 min using a 50 kDa centrifugal filter.

Hemolysis assay. Fresh blood from mice was obtained in heparinized tubes, centrifuged the mixture at 3000 rpm for 10 min, and followed by adding 20% PBS (v/v). **Ru1085** NPs with various concentrations were dissolved in PBS. Water was used as a positive control, while PBS served as a negative control. After incubation

for 1 h, the suspension was centrifuged at 3000 rpm for 5 min. The absorbance at 540 nm was recorded for each sample. The hemolysis assay was calculated using the following formula:

$$\text{Hemolysis Rate(\%)} = \frac{\text{OD}_{\text{sample}} - \text{OD}_{\text{PBS}}}{\text{OD}_{\text{water}} - \text{OD}_{\text{PBS}}} \times 100\% \quad (7)$$

Animals and tumor model. All animal experiments involved in this study were conducted in accordance with the Guide for the Care and Use of Laboratory Animals of Central China Normal University. To establish xenografted tumor models, Balb/c nude mice (female, 5 weeks) were subcutaneously injected with A549 cell suspension (1×10^6 cells).

Pharmacokinetics. The A549 tumor-bearing mice were intravenously injected with Ru1085 NPs (1 mg Ru/kg). Mice ($n = 3$) were sacrificed at various time points after administration. Blood was collected by eyeball extirpating and kept in heparinized tubes. The amount of Ru in plasma was then measured by ICP-MS.

In vivo NIR-II fluorescence imaging-guided and monitored antitumor experiments. After the tumor reached to $\sim 100 \text{ mm}^3$, the tumor models were intravenously injected with Ru1085 NPs (1 mg Ru/kg), and NIR-II fluorescence images (808 nm, 1000 LP, 0.05 W cm^{-2} , and 200 ms) were taken using a in vivo NIR-II fluorescence imaging system. For the therapeutic experiments, the tumor models were separated into five groups ($n = 5$), including: (1) Ru1085 NPs (1 mg Ru/kg) plus laser, (2) Ru1085 NPs (1 mg Ru/kg), (3) cisplatin (1 mg Pt/kg), (4) PBS plus laser, and (5) PBS. At 24 h post-injection, the tumors (group 1 and 4) were illustrated with 808 nm laser (0.8 W cm^{-2} , 10 min) and the temperature was monitored by an IR thermal camera. The NIR-II fluorescence images (808 nm, 1000 LP, 0.05 W cm^{-2} , and 200 ms) were taken at various time points till 5 days. The tumor volume and body weight were recorded every 2 days. After 20 days, major organs, tumor and blood were collected to make H&E staining and blood biochemistry analysis.

Statistical analysis. Data were presented as means \pm standard deviation (s.d.). The sample number (n) indicates the number of independent biological samples in each experiment. Statistical differences were compared by unpaired Student's t -tests analyzing used GraphPad Prism 6 software.

Reporting summary. Further information on research design is available in the Nature Research Reporting Summary linked to this article.

Data availability

The authors declare that the data supporting the findings of this study are available within the paper and its supplementary information files. Data were available from the corresponding author upon request.

Received: 5 November 2021; Accepted: 22 March 2022;

Published online: 14 April 2022

References

- Johnstone, T. C., Suntharalingam, K. & Lippard, S. J. The next generation of platinum drugs: targeted Pt(II) agents, nanoparticle delivery, and Pt(IV) prodrugs. *Chem. Rev.* **116**, 3436–3486 (2016).
- Wang, X., Jin, S., Muhammad, N. & Guo, Z. Stimuli-responsive therapeutic metalodrugs. *Chem. Rev.* **119**, 1138–1192 (2019).
- Zeng, L. et al. The development of anticancer ruthenium(II) complexes: from single molecule compounds to nanomaterials. *Chem. Soc. Rev.* **46**, 5771–5804 (2017).
- Betzanos-Lara, S., Salassa, L., Habtemariam, A. & Sadler, P. J. Photocontrolled nucleobase binding to an organometallic Ru(II) arene complex. *Chem. Commun.* **43**, 6622–6624 (2009).
- Poynton, F. E. et al. The development of ruthenium(II) polypyridyl complexes and conjugates for in vitro cellular and in vivo applications. *Chem. Soc. Rev.* **46**, 7706–7756 (2017).
- Notaro, A. & Gasser, G. Monomeric and dimeric coordinatively saturated and substitutionally inert Ru(II) polypyridyl complexes as anticancer drug candidates. *Chem. Soc. Rev.* **46**, 7317–7337 (2017).
- Li, A., Turro, C. & Kodanko, J. J. Ru(II) polypyridyl complexes derived from tetradentate ancillary ligands for effective photocaging. *Acc. Chem. Res.* **51**, 1415–1421 (2018).
- Karges, J. et al. Rationally designed ruthenium complexes for 1- and 2- photon photodynamic therapy. *Nat. Commun.* **11**, 3262 (2020).
- Huang, H. et al. Highly charged ruthenium(II) polypyridyl complexes as lysosome-localized photosensitizers for two-photon photodynamic therapy. *Angew. Chem. Int. Ed.* **54**, 14049–14052 (2015).
- Heinemann, F., Karges, J. & Gasser, G. Critical overview of the use of Ru(II) polypyridyl complexes as photosensitizers in one-photon and two-photon photodynamic therapy. *Acc. Chem. Res.* **50**, 2727–2736 (2017).
- Paul, S. et al. Ruthenium(II) conjugates of boron-dipyrromethene and biotin for targeted photodynamic therapy in red light. *Inorg. Chem.* **59**, 913–924 (2020).
- Karges, J. et al. Rationally designed long-wavelength absorbing Ru(II) polypyridyl complexes as photosensitizers for photodynamic therapy. *J. Am. Chem. Soc.* **142**, 6578–6587 (2020).
- Raza, A. et al. A dinuclear Ruthenium(II) complex excited by near-infrared light through two-photon absorption induces phototoxicity deep within hypoxic regions of melanoma cancer spheroids. *J. Am. Chem. Soc.* **142**, 4639–4647 (2020).
- Qiu, K., Chen, Y., Rees, T. W., Ji, L. & Chao, H. Organelle-targeting metal complexes: from molecular design to bio-applications. *Coord. Chem. Rev.* **378**, 66–86 (2019).
- Karges, J., Yempala, T., Tharaud, M., Gibson, D. & Gasser, G. A multi-action and multi-target Ru^{II}-Pt^{IV} conjugate combining cancer-activated chemotherapy and photodynamic therapy to overcome drug resistant cancers. *Angew. Chem. Int. Ed.* **59**, 7069–7075 (2020).
- Maeda, H. The enhanced permeability and retention (EPR) effect in tumor vasculature: the key role of tumor-selective macromolecular drug targeting. *Adv. Enzym. Regul.* **22**, 189–207 (2001).
- Wolinsky, J. B. & Grinstaff, M. W. Therapeutic and diagnostic applications of dendrimers for cancer treatment. *Adv. Drug. Deliv. Rev.* **60**, 1037–1055 (2008).
- Vajpayee, V. et al. Self-assembly of cationic, hetero- or homonuclear Ruthenium (II) macrocyclic rectangles and their photophysical, electrochemical, and biological studies. *Organometallics* **30**, 6482–6489 (2011).
- Cook, T. R. & Stang, P. J. Recent developments in the preparation and chemistry of metallacycles and metallacages via coordination. *Chem. Rev.* **115**, 7001–7045 (2015).
- Casini, A., Woods, B. & Wenzel, M. The promise of self-assembled 3D supramolecular coordination complexes for biomedical applications. *Inorg. Chem.* **56**, 14715–14729 (2017).
- Xia, D. et al. Functional supramolecular polymeric networks: the marriage of covalent polymers and macrocycle-based host-guest interactions. *Chem. Rev.* **120**, 6070–6123 (2020).
- Bhattacharyya, S. et al. Self-assembled Pd₁₂ coordination cage as photoregulated oxidase-like nanozyme. *J. Am. Chem. Soc.* **142**, 18981–18989 (2020).
- Tuo, W. et al. Biomedical applications of Pt(II) metallacycles/metallacages-based agents: from mono-chemotherapy to versatile imaging contrasts and theranostic platforms. *Coord. Chem. Rev.* **443**, 214017 (2021).
- Zhu, J. et al. Switchable organoplatinum metallacycles with high quantum yields and tunable fluorescence wavelengths. *Nat. Commun.* **10**, 4285 (2019).
- Zhou, Z. et al. A self-assembled Ru-Pt metallacage as a lysosome-targeting photosensitizer for 2-photon photodynamic therapy. *Proc. Natl Acad. Sci. USA* **116**, 20296–20302 (2019).
- Singh, N. et al. Coordination-driven self-assembly and anticancer potency studies of ruthenium-cobalt-based heterometallic rectangles. *Chem. Eur. J.* **22**, 16157–16164 (2016).
- Adeyemo, A. A., Shettar, A., Bhat, I. A., Kondaiah, P. & Mukherjee, P. S. Self-assembly of discrete Ru^{II}₈ molecular cages and their in vitro anticancer activity. *Inorg. Chem.* **56**, 608–617 (2017).
- Adeyemo, A. A., Shettar, A., Bhat, I. A., Kondaiah, P. & Mukherjee, P. S. Coordination-driven self-assembly of ruthenium(II) architectures: synthesis, characterization and cytotoxicity studies. *Dalton. Trans.* **47**, 8466–8475 (2018).
- Starha, P. Multinuclear biologically active Ru, Rh, Os and Irarene complexes. *Coord. Chem. Rev.* **431**, 213690–213737 (2021).
- Jo, J. H. et al. Coordination-driven self-assembly using ditopic pyridyl-pyrazole donor and *p*-cymene Ru(II) acceptors: [2]catenane synthesis and anticancer activities. *Inorg. Chem.* **56**, 8430–8438 (2017).
- Zhou, Z. et al. Heterometallic Ru-Pt metallacycle for two-photon photodynamic therapy. *Proc. Natl Acad. Sci. USA* **116**, 5664–5669 (2019).
- Yan, X., Cook, T. R., Wang, P., Huang, F. & Stang, P. J. Highly emissive platinum(II) metallacages. *Nat. Chem.* **7**, 342–348 (2015).
- Li, Y. et al. Giant concentric metallosupramolecule with aggregation-induced phosphorescent emission. *J. Am. Chem. Soc.* **142**, 14638–14648 (2020).
- Qin, Y. et al. Light-controlled generation of singlet oxygen within a discrete dual-stage metallacycle for cancer therapy. *J. Am. Chem. Soc.* **141**, 8943–8950 (2019).
- Li, J. et al. Recent advances in the development of NIR-II organic emitters for biomedicine. *Coord. Chem. Rev.* **415**, 213318–213331 (2020).

36. Hong, G., Antaris, A. L. & Dai, H. Near-infrared fluorophores for biomedical imaging. *Nat. Biomed. Eng.* **1**, 0010–0032 (2017).
37. Xu, C. & Pu, K. Second near-infrared photothermal materials for combinational nanotheranostics. *Chem. Soc. Rev.* **50**, 1111–1137 (2021).
38. He, S., Song, J., Qu, J. & Cheng, Z. Crucial breakthrough of second near-infrared biological window fluorophores: design and synthesis toward multimodal imaging and theranostics. *Chem. Soc. Rev.* **47**, 4258–4278 (2018).
39. Lu, L. et al. NIR-II bioluminescence for in vivo high contrast imaging and in situ ATP-mediated metastases tracing. *Nat. Commun.* **11**, 4192 (2020).
40. Cai, Y. et al. Optical nano-agents in the second near-infrared window for biomedical applications. *Chem. Soc. Rev.* **48**, 22–37 (2019).
41. Li, C., Chen, G., Zhang, Y., Wu, F. & Wang, Q. Advanced fluorescence imaging technology in the near-infrared-II window for biomedical applications. *J. Am. Chem. Soc.* **142**, 14789–14804 (2020).
42. Zhou, H. et al. Upconversion NIR-II fluorophores for mitochondria-targeted cancer imaging and photothermal therapy. *Nat. Commun.* **11**, 6183 (2020).
43. Liu, Y. et al. Versatile types of inorganic/organic NIR-IIa/IIb fluorophores: from strategic design toward molecular imaging and theranostics. *Chem. Rev.* **122**, 209–268 (2022).
44. Zhao, Y. et al. Self-assembled ruthenium (II) metallacycles and metallacages with imidazole-based ligands and their in vitro anticancer activity. *Proc. Natl Acad. Sci. USA* **116**, 4090–4098 (2019).
45. Dai, Y. et al. Multifunctional thermosensitive liposomes based on natural phase-change material: near-infrared light-triggered drug release and multimodal imaging-guided cancer combination therapy. *ACS Appl. Mater. Interfaces* **11**, 10540–10553 (2019).
46. Zheng, Y. et al. All-in-one mitochondria-targeted NIR-II fluorophores for cancer therapy and imaging. *Chem. Sci.* **12**, 1843–1850 (2021).
47. Yang, L. et al. ICG-conjugated and ¹²⁵I-labeled polymeric micelles with high biosafety for multimodality imaging-guided photothermal therapy of tumors. *Adv. Healthc. Mater.* **9**, 1901616–1901629 (2020).
48. Refsgaard, H. H. F. et al. In silico prediction of membrane permeability from calculated molecular parameters. *J. Med. Chem.* **48**, 805–811 (2005).
49. Greenhalgh, C. J. et al. Exploration of matrix effects in laser ablation inductively coupled plasma mass spectrometry imaging of cisplatin-treated tumors. *Anal. Chem.* **92**, 9847–9855 (2020).
50. Yu, G. et al. Porphyrin nanocage-embedded single-molecular nanoparticles for cancer nanotheranostics. *Angew. Chem. Int. Ed.* **58**, 8799–8803 (2019).
51. Thomas, A. P., Palanikumar, L., Jeena, M. T., Kim, K. & Ryu, J. H. Cancer-mitochondria-targeted photodynamic therapy with supramolecular assembly of HA and a water soluble NIR cyanine dye. *Chem. Sci.* **8**, 8351–8356 (2017).
52. Fulda, S., Galluzzi, L. & Kroemer, G. Targeting mitochondria for cancer therapy. *Nat. Rev. Drug Discov.* **9**, 447–464 (2010).
53. Jee, C. D. et al. Loss of caspase-1 gene expression in human gastric carcinomas and cell lines. *Int. J. Oncol.* **26**, 1265–1271 (2005).
54. Dyson, P. J. & Sava, G. Metal-based antitumour drugs in the post genomic era. *Dalton Trans.* **16**, 1929–1933 (2006).
55. Ma, L. et al. A cancer cell-selective and low-toxic bifunctional heterodinuclear Pt(IV)-Ru(II) anticancer prodrug. *Inorg. Chem.* **57**, 2917–2924 (2018).
56. Ryan, R. T. et al. Bis-tridentate N-heterocyclic carbene Ru(II) complexes are promising new agents for photodynamic therapy. *Inorg. Chem.* **59**, 8882–8892 (2020).
57. Duan, H. & Nie, S. Cell-penetrating quantum dots based on multivalent and endosome-disrupting surface coatings. *J. Am. Chem. Soc.* **129**, 3333–3338 (2007).
58. Gasparini, G., Bang, E.-K., Montenegro, J. & Matile, S. Cellular uptake: lessons from supramolecular organic chemistry. *Chem. Commun.* **51**, 10389–10402 (2015).
59. Sansone, F. et al. DNA condensation and cell transfection properties of guanidinium calixarenes: dependence on macrocycle lipophilicity, size, and conformation. *J. Am. Chem. Soc.* **128**, 14528–14536 (2006).
60. Ortel, B., Shea, C. R. & Calzavara-Pinton, P. Molecular mechanisms of photodynamic therapy. *Front. Biosci.* **14**, 4157–4172 (2009).
61. Chen, C. et al. High cell selectivity and low-level antibacterial resistance of designed amphiphilic peptide G(IKK)₃I-NH₂. *ACS Appl. Mater. Interfaces* **6**, 16529–16536 (2014).

Acknowledgements

This work was supported by National Natural Science Foundation of China (NSFC 22022404, 22074050, and 22125106), Wuhan Scientific and Technological Projects (2019020701011441), the State Key Laboratory of Materials-Oriented Chemical Engineering (KL20-05), the Open Fund of Guangdong Provincial Key Laboratory of Luminescence from Molecular Aggregates, Guangzhou 510640, China (South China University of Technology, 2020-k11ma-06), and the Developmental Fund for Science and Technology of Shenzhen (RCJC20200714114556306).

Author contributions

Y.S. conceived the project and designed the experiments. Y.X., C.L., Shuai Lu, X.Y., and X.L. designed, synthesized, and characterized the materials. Z.W. carried out the theoretical calculations. Y.X., C.L., and Shuang Liu performed the in vitro and in vivo study. Y.X., X.L., and Y.S. wrote the manuscript. All authors analyzed and discussed the results and have given approval to the final version of the manuscript.

Competing interests

The authors declare no competing interests.

Additional information


Supplementary information The online version contains supplementary material available at <https://doi.org/10.1038/s41467-022-29572-2>.

Correspondence and requests for materials should be addressed to Xiaopeng Li or Yao Sun.

Peer review information *Nature Communications* thanks Deju Ye and the other anonymous reviewers for their contribution to the peer review of this work. Peer reviewer reports are available.

Reprints and permission information is available at <http://www.nature.com/reprints>

Publisher's note Springer Nature remains neutral with regard to jurisdictional claims in published maps and institutional affiliations.

 **Open Access** This article is licensed under a Creative Commons Attribution 4.0 International License, which permits use, sharing, adaptation, distribution and reproduction in any medium or format, as long as you give appropriate credit to the original author(s) and the source, provide a link to the Creative Commons license, and indicate if changes were made. The images or other third party material in this article are included in the article's Creative Commons license, unless indicated otherwise in a credit line to the material. If material is not included in the article's Creative Commons license and your intended use is not permitted by statutory regulation or exceeds the permitted use, you will need to obtain permission directly from the copyright holder. To view a copy of this license, visit <http://creativecommons.org/licenses/by/4.0/>.

© The Author(s) 2022